Cell Reports
Physical Science

CellPress
OPEN ACCESS

Article

Imaging local luminescence variations in $CdSe_{0.1}Te_{0.9}$ thin films grown by the colossal grain growth process

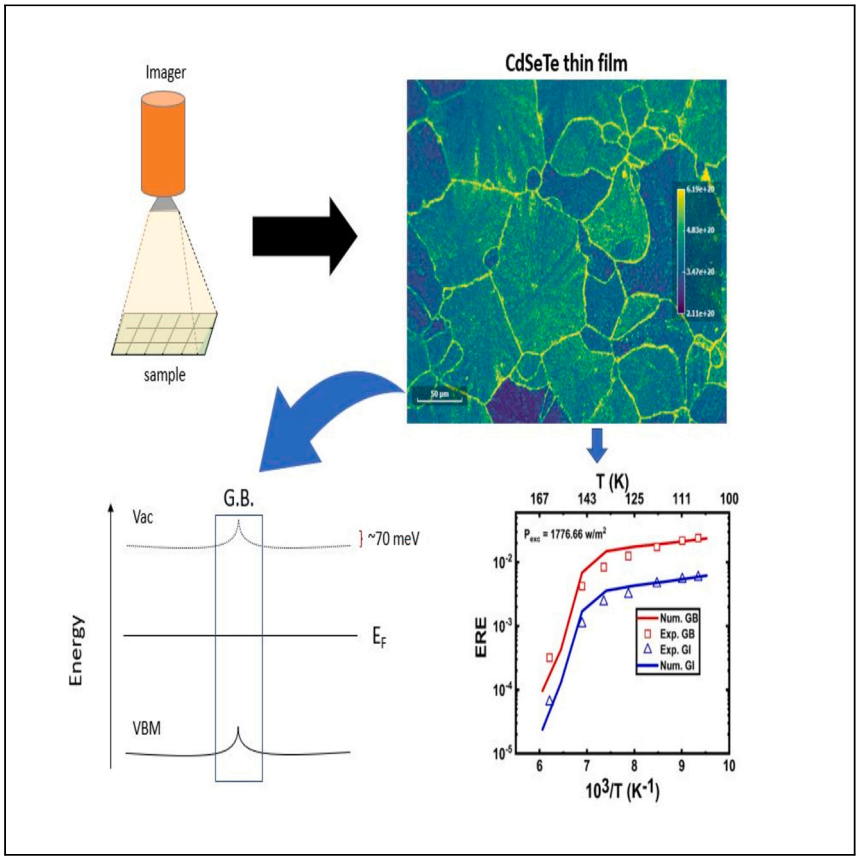

Visualizing and studying local charge carrier recombination phenomena in polycrystalline thin films is crucial for a better understanding of factors that limit the PCE of solar cells. Here, Neupane et al. investigate the luminescence properties of grain boundaries and grain interiors and the local band structure in CdSeTe films grown by the CGG process.

Ganga R. Neupane, Andrew J. Winchester, Nicolas Marquez Peraca, ..., Sujitra J. Pookpanratana, Susanna M. Thon, Behrang H. Hamadani

behrang.hamadani@nist.gov

Highlights

CdSeTe thin films have a non-uniform local structure and charge carrier recombination

PL imaging reveals sub-bandgap energetic disorder, impurity DA-type transitions

PEEM confirms an upward band bending at the grain boundaries

PL thermal quenching was observed at both grains and grain boundaries

Neupane et al., Cell Reports Physical Science 4, 101522
August 16, 2023
https://doi.org/10.1016/j.xcrp.2023.101522

Cell Reports
Physical Science

CellPress
OPEN ACCESS

Article

Imaging local luminescence variations in $CdSe_{0.1}Te_{0.9}$ thin films grown by the colossal grain growth process

Ganga R. Neupane,[1,3] Andrew J. Winchester,[2] Nicolas Marquez Peraca,[4] David S. Albin,[5] Joel N. Duenow,[5] Matthew O. Reese,[5] Sujitra J. Pookpanratana,[2] Susanna M. Thon,[3] and Behrang H. Hamadani[1,6,*]

SUMMARY

Clear visualization and understanding of luminescence properties of grain interiors and grain boundaries in polycrystalline thin-film photovoltaic materials are crucial to achieving high-performance solar cells. Luminescence-based measurements, for example, reveal sub-bandgap energetic disorder or impurity-related radiative transitions in these materials, and when performed in the absolute scale, they can show the extent of voltage-limiting non-radiative recombination. Here we use a hyperspectral imaging technique to investigate inter- and intra-grain photoluminescence variations in polycrystalline $CdSe_{0.1}Te_{0.9}$ films made by the colossal grain growth process. We observe that grain boundaries show higher luminescence than grain interiors for all energies below the bandgap energy. Multiple distinct sub-bandgap defect transitions are detected and determined to be related to donor-acceptor pair impurities. A comparison of the excitation-intensity-dependent photoluminescence at the grain boundaries with grain interiors suggests that carrier concentration is higher at grain boundaries. This finding is supported by photoemission electron microscopy imaging of the films, showing ≈70 meV upward energy shift in the band structure at the grain boundaries. Finally, we investigate a dramatic thermal quenching behavior related to the donor-acceptor pairs luminescence over a temperature range and use a rate-equation model to attribute it to the sudden redirection of the radiative recombination channels to non-radiative channels with increasing temperature.

INTRODUCTION

Thin-film CdTe-based solar cells are gaining renewed interest in recent years due to significant improvements in charge carrier lifetimes by alloying CdTe with selenium (Se), resulting in steady improvements in their power conversion efficiency (PCE).[1] It is believed that Se incorporation in CdTe increases the photocurrent by reducing the bandgap and passivating defects that would otherwise act as non-radiative recombination centers.[2] Despite these gains, solar cell efficiencies remain below the theoretical limit due to low open circuit voltage, V_{oc}, compared to the Shockley-Queisser limit. Some of the limiting factors for the V_{oc} are thought to be the grain size and high defect densities within the material.[3,4] Small-grained films that are typically grown by deposition techniques such as vapor transport deposition or close-spaced sublimation have grain size/film thickness ratios close to one (i.e., a micrometer-thick film

[1]Engineering Laboratory, National Institute of Standard &Technology, Gaithersburg, MD 20899, USA

[2]Physical Measurements Laboratory, National Institute of Standard &Technology, Gaithersburg, MD 20899, USA

[3]Department of Electrical and Computer Engineering, Johns Hopkins University, Baltimore, MD 21218, USA

[4]Department of Physics & Astronomy, Rice University, Houston, TX 77005, USA

[5]National Renewable Energy Laboratory, Golden, CO 80401, USA

[6]Lead contact

*Correspondence: behrang.hamadani@nist.gov

https://doi.org/10.1016/j.xcrp.2023.101522

with micrometer-sized grains).[5] Often, micrometer-sized grains are only obtained from film recrystallization after the $CdCl_2$ treatment during the cell fabrication process. Annealing CdTe films in $CdCl_2$ not only increases the grain sizes but also passivates grain boundary (GB) defects. These larger grains and passivated GBs have been shown to result in better charge collection.[6,7] However, despite the ubiquity of the $CdCl_2$ treatment and its many positive effects, there is a concern that it may need to be avoided due to carrier compensation, which can limit hole activation or introduce undesirable potential fluctuations.[5]

Several studies[8,9] have reported that the deep bandgap defects related to cadmium vacancies (V_{Cd}) act as major non-radiative recombination centers in CdTe thin films. Hence to passivate these defects, $CdCl_2$ treatment and alloying CdTe with Se are helpful.[8,10] However, growth techniques that can produce very large grains with low defect densities and minimal or no $CdCl_2$ treatment have been viewed as the next area of development. The colossal grain growth (CGG) method, also referred to as the explosive recrystallization method, is a promising post-deposition process that has been shown to produce CdSeTe films with grain sizes approaching 1 mm without a $CdCl_2$ treatment.[5] Unlike the traditional growth techniques, this method can produce thin films having grain-size-to-thickness ratios greater than 100. Currently, these films are targeted to be used as templates for epitaxial growth of similarly large-grained CdTe thin films instead of serving as the active layer themselves in a device structure because they seem to grow under a very narrow process window. However, very early evidence[11,12] suggests that growth of giant-grained films alone may not be enough to produce high-quality devices, and other passivation treatments including $CdCl_2$ treatment may still be needed to mitigate the negative effect of defects. It is important to understand how the $CdCl_2$ treatment and incorporation of Se in CdTe affect the properties of grain interiors (GIs) and GBs in different ways. Recent studies have shown that segregation of Cl and Se at the boundaries can shift the deep interface states to shallower states, i.e., toward the valence/conduction band maxima/minima (VBM/CBM),[1,2] thus reducing the non-radiative recombination rates.

Hyperspectral (HS) photoluminescence (PL) imaging is a fast, non-destructive, and contactless technique to study defects and luminescence variations in thin-film semiconductors with micrometer spatial and high spectral resolution.[13,14] This tool captures a deck of images, called the image cube, by acquiring signals over a chosen spectral range. Unlike traditional imaging systems, detailed spectral information is captured for every single pixel within the image. Through a radiometric calibration process, the raw luminescence signal can be converted to the actual photon emission rates (i.e., photon flux as the number of photons per unit area per second per unit energy), which helps determine different local physical properties of the material, such as the local quasi-Fermi level splitting energy, $\Delta\mu$, and the external radiative efficiency (ERE). In materials with significant inhomogeneity, such as granular polycrystalline materials, this technique can be used to elucidate the influence of GBs on electronic charge transport. When hyperspectral PL imaging is performed over a temperature range,[15] it can reveal transitions through different sub-bandgap states at the local level. Since both radiative and non-radiative transitions can take place depending on the specific temperature range, sometimes even resulting in abrupt PL quenching behavior over a very small temperature range, it is imperative that PL images are obtained as a function of temperature. Several reports have explained unusual PL quenching behavior in semiconductors using different empirical models.[15,16] However, these models cannot always satisfactorily address the physical origins of superlinear and tunable

PL response in materials such as InGaAsP/InP. Therefore, a new model (rate equation) was proposed recently to provide a better physical origin for these sorts of PL quenching behavior.[17]

In this work, we have performed a comprehensive, temperature-dependent, hyperspectral PL imaging study on CGG $CdSe_{0.1}Te_{0.9}$ polycrystalline films. The large grains and clearly defined boundaries in thin films of this material make it a very nice candidate for visualizing carrier recombination effects and sub-bandgap defect properties under an optical microscope. We investigated the local PL emission variability by carefully selecting and studying the GI and GB pixels of these images and comparing them with each other. From these images, we extracted the $\Delta\mu$ variations across the grains and the GBs and show that local potential fluctuations of up to $\approx$20 meV can be observed in this material system. Several types of radiative sub-bandgap transitions were observed, in both the GIs and GBs, and were associated with donor-acceptor pair (DAP) transitions. Excitation-intensity-dependent PL images indirectly imply that carrier density is higher at the GBs than in the GIs, consistent with complementary photoemission electron microscopy (PEEM) imaging of the electronic structure at the GBs. In addition, an interesting, not previously reported thermal quenching of the sub-bandgap DAP luminescence was observed at both the GB and GIs, resulting in many orders of magnitude of change in the luminescence photon flux over a narrow temperature domain. This quenching behavior was explained relatively well with a rate-equation model that properly accounts for the DAP and non-radiative transitions. Our work demonstrates that complementary imaging techniques on unfinished device structures can help shed light on carrier recombination phenomena in disordered material systems. The knowledge learned from these visual techniques will ultimately drive improvements in material processing and growth techniques that will lead to better device performance.

RESULTS AND DISCUSSION

Hyperspectral PL imaging system and the samples

Figure 1A and 1B show the schematics depicting the operation of the hyperspectral PL imaging system and its main components. The hyperspectral filter box contains the gratings used to spectrally image the sample and obtain an image cube, which consists of a series of images over a range of wavelengths. A visible-range scientific complementary metal-oxide-semiconductor (sCMOS) camera is used to capture the images for the data shown in this work. The acquisition time for an image cube depends on the integration time and wavelength steps. The light excitation for the PL is provided by a 532-nm laser over the entire field of view of the objective, therefore allowing for a uniform illumination of the sample. More details are provided in the section "experimental procedures."

An optical image of an area of the CdSeTe thin films used in this study is shown in Figure 1C and reveals a polycrystalline structure with a variety of grain sizes and clearly defined GBs. We investigate the PL characteristics of the GIs and GBs in the following section. The films investigated here are all $CdCl_2$ treated to improve the luminescence properties because untreated films of this material give very low luminescence despite the large grain sizes.

Temperature-dependent PL imaging

We first turn our attention to what the PL images reveal at several temperatures. At the lowest temperatures achieved, the observed photon flux is very high, even under a very low laser illumination intensity, and very clear images are

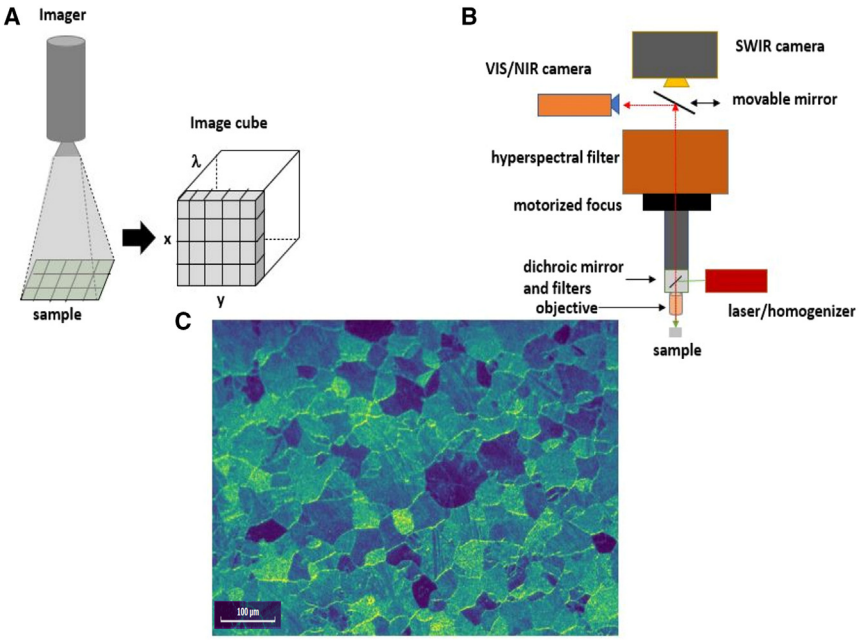

Figure 1. Schematics representing operation of hyperspectral PL imaging system

(A) System creates the image cube, a combination of the spectral (λ) data with spatial (x,y) one, which is a stack of images that a sample generates.

(B) Different components of the hyperspectral imaging system.

(C) Optical image of CdSeTe thin film.

obtained. The spectra of the PL maps consist of several distinct peaks in the energy range ≈1.2 to 1.6 eV (shown in Figure 4), with a very large emission peak at 1.32 eV. Several PL images at this energy and at a fixed laser intensity of ≈1,800 W/m^2 are shown in Figures 2A–2F. The images show a variety of grain sizes, including some large ones (100 to 200 μm) and clear, prominent GBs with higher luminescence flux compared to GIs. Since these films are $CdCl_2$ passivated, a higher radiative emission at the GBs is consistent with the notion that Se and Cl_2 treatment reduces the non-radiative recombination overall but more so at the GBs. The effect of Se and Cl at the GBs of CdTe thin films has been reported in various studies using density functional theory calculations,[1,18] suggesting that the co-doping of Se and Cl reduces the depth and density of mid-gap states, which otherwise act as non-radiative recombination centers. In addition, luminescence is strongest at the lowest temperatures (107 K), as shown in Figure 2A, and sharply decreases with the increase in temperature up to 161 K as seen by substantial reductions in the photon flux. With increasing temperature, the capture cross section of non-radiative channels increases substantially relative to radiative channels, and non-radiative recombination dominates, hence reducing the intensity of PL from all locations. The PL quenching behavior for both the GBs and GIs are similar, as shown in Figure S2. We will discuss this quenching behavior in more detail later.

In addition to GB vs. GI variations, grain-to-grain variations are also observed. Some grains, for example, are significantly darker than their surroundings in the PL images, suggesting that either higher local defect concentrations or unpassivated interfacial/surface defects are present. Based on these luminescence variations, we estimate most grain-to-grain energy fluctuation on the order of ≈10 meV, but differences as high as ≈ 20 meV have also been observed. We arrive at these estimated values by comparing our data against a density-of-states-based

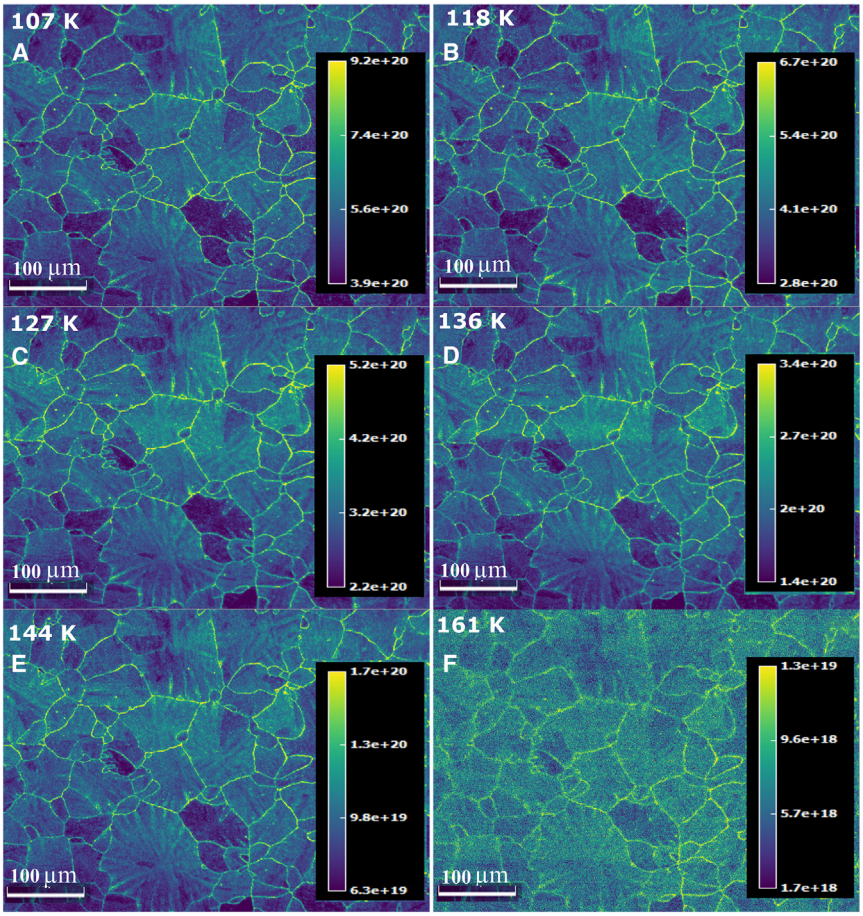

Figure 2. Temperature-dependent PL maps

(A–F) Spatial maps of the temperature dependence of absolute PL flux in photons/(m^2 s eV) (color bar) for a CGG $CdSe_{0.1}Te_{0.9}$ polycrystalline film taken at different temperatures from 107 to 161 K at a fixed wavelength of 940 nm (1.32 eV) and fixed laser intensity (1,776 W/m^2).

PL model developed by Katahara and Hillhouse[19] that incorporates $\Delta\mu$ and the absorption coefficient of the material. Figure 3 shows a map of $\Delta\mu$ variations, constructed with values obtained from the Katahara model, for an area of the film at 201 K and under an incident excitation intensity of 97 kW/m^2 (i.e., ~100 suns). More detail is provided in Tables S1, S2, and S3; Figure S4; and Notes S1, S2, S3, and S4, including information on the local variations of several other model parameters. These $\Delta\mu$ grain-to-grain variations suggest non-uniform defect passivation by $CdCl_2$ treatment. From the map, it is also clear that the $\Delta\mu$ values are higher at GBs compared to GIs, consistent with the earlier assertion that GBs are better passivated.

Also, some interesting striations are observed across the interior of the larger grains, showing radial features from the center toward the boundary indicating a heterogeneous pattern of carrier recombination within a single grain. We believe these intragranular variations are related to changes in the crystalline orientation of the grains. In very large or fast-growth grains, as the radius of the grain increases, a point is reached where lattice strain causes a large orientation shift in the growing crystal; this feature is particular to CGG films. An example of this is the boundary between regions 2 and 3 revealed by the change in color shown Figure S1. These types of

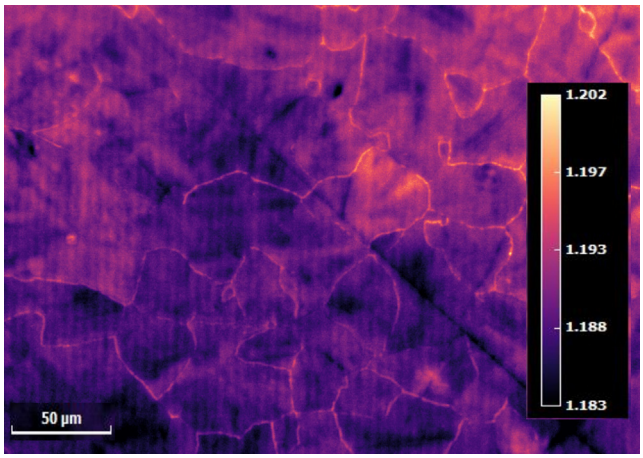

Figure 3. Map of the quasi-Fermi level splitting energy

Map of quasi-Fermi level splitting energy ($\Delta\mu$) variations across a region of the film, estimated from the absolute PL emission rate maps at 201 K under an excitation intensity of 97 kW/m^2. The color bar shows the values of $\Delta\mu$ in eV.

striations are less visible in regions of the film where the grain sizes are smaller (i.e., ≈30–80 µm) compared to grains >100 µm in size.

Spectral-dependent PL imaging

Figure 4 shows several PL flux maps at different wavelengths. These images were taken at a fixed excitation intensity of 97.4 kW/m^2 at 201 K. We chose these wavelengths based on the PL spectra shown in Figure 5, with an attempt to pick wavelengths that are located on the low- or high-energy side of a given local peak. From the images, we can see that GI and GB contributions are clearly wavelength dependent. At shorter wavelengths (i.e., $\lambda \approx 830$ nm or shorter), as shown in Figure 4A, it is hard to distinguish between GIs and GBs. The PL spectra in Figure 5 clearly show the overlap of the PL GB and GI emission spectra in the tail region E > 1.49 eV. These spectra have been constructed from the sample mean of 10 GIs and 10 GBs, each selected carefully over a range of pixels using a precise selection tool within the image analysis software (PHySpec 2.26.9). The collapse of the high-energy tail of the GB and GI spectra means that GBs become harder to distinguish from GIs in the images. The peak observed at 1.49 eV is indeed the band-to-band (BB) optical transition for this material, as explained next, and this photon energy is roughly equal to E_g at this temperature. However, the GB and GI emission rates diverge for all energies <1.49 eV, with the GBs consistently showing higher PL signals. This is the reason the GBs appear brighter in all the images (Figure 4B–4F), with the brightest contrast appearing at energies where the GB and GI spectra diverge the most from each other, such as at 1.4 eV (886 nm) or 1.29 eV (960 nm).

It has been reported that $\sum$3 (112) GBs with a Te core are the dominant GBs in CdTe thin films and are responsible for deep states.[20,21] These mid-gap states act as nonradiative recombination centers and reduce the radiative emission rates. However, the segregation of Se and Cl at GBs favors the substitution of Te and partially passivates these states.[22,23] It has also been reported that the probability of Se substituting Te at GB sites is at least twice as much at the grain interior.[1] This is likely the reason why we see more luminescence at GBs than GIs in Se-alloyed CdTe thin film with $CdCl_2$ treatment.

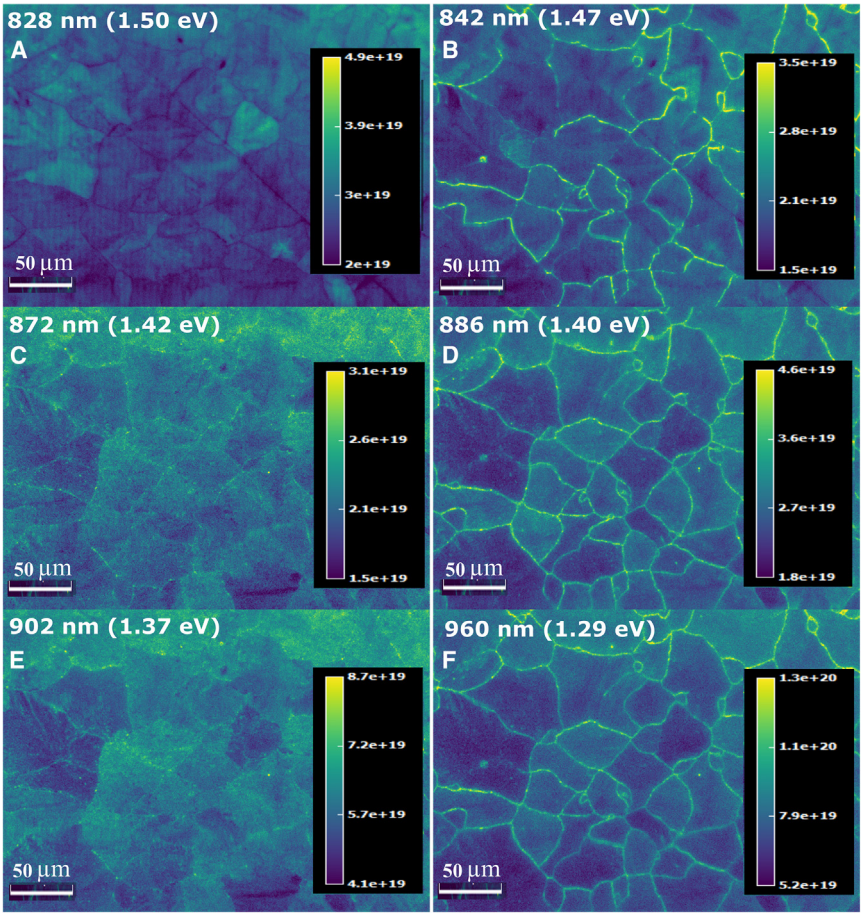

Figure 4. Wavelength/energy-dependent absolute PL images

(A–F) PL images in photons/(m^2 s eV) showing alternate GI and GB contributions at fixed intensity (97.4 kW/m^2) and at fixed temperature (201 K).

All other PL peaks that are observed in the energy range shown in Figure 5 are related to sub-bandgap impurity defect transitions (DAP transitions, discussed below) and are present at both GBs and GIs. The PL peaks appear broader at the GB sites, compared to the GIs. This extra energetic disorder at the GB is expected because the crystalline structure is disturbed at the boundaries and, furthermore, GBs have been shown to contain more impurities.[24] The higher PL signal from the GBs suggests that although sub-bandgap radiative transitions benefit more from Cl passivation of non-radiative centers at the GBs than the GIs, the higher-energy BB transitions are not afforded a similar enhancement at the GBs. We therefore conclude that the shallower donor-acceptor states, which constitute these sub-gap emission peaks, are more sensitive to the presence of mid-gap, deep states than carriers from the bands, a finding that is consistent with the rate-equation model discussed later.

The BB transition

Estimating the actual temperature of the CdSeTe film on glass inside the cryostat under laser illumination is challenging. Near room temperature, specifically, the radiative efficiency of the material is very low (ERE $\approx 10^{-7}$), and so a large laser excitation intensity (close to 100 suns equivalent) is needed to observe a reasonable PL signal. It is possible to estimate the film temperature by tracking the

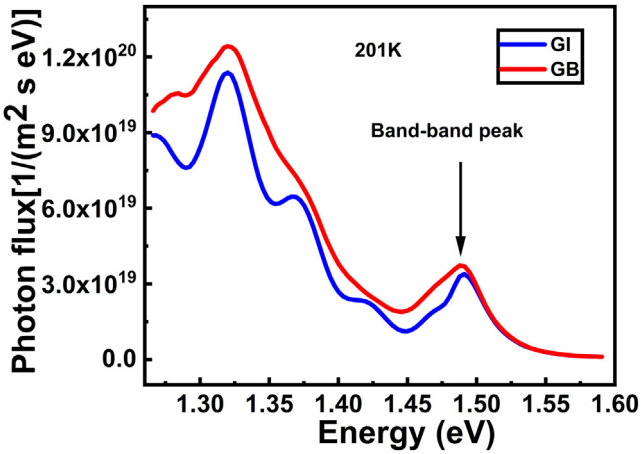

Figure 5. PL spectra for GI and GB

Absolute PL flux in photons/(m^2 s eV) versus energy, showing representative spectra for GBs (red) and grain interiors (blue).

highest energy peak, assumed to be the BB transition, as the sample is cooled down from room temperature and seeing whether it tracks the Varshni relationship[25] with constants published previously for CdTe. We calculated the bandgap energies as a function of temperature by fitting the BB spectra to the PL model of Katahara and Hillhouse[19] for both the GBs and the GIs in the temperature range from 304 to 201 K. For the lower temperature range (107–161 K) the defect peaks are so dominant that it becomes hard to reliably fit the small BB peak to the Katahara model. We therefore approximated the E_g in this range by fitting it to a Gaussian peak and extracting the center energy as E_g. This variation of the E_g energy with temperature is shown in Figure 6.The Varshni relationship for the variation of the band gap energy E_g with temperature T in semiconductors is given by Equation 1:

$$E_g = E_0 - \frac{\alpha T^2}{T+\beta} \qquad \text{(Equation 1)}$$

where α (6.323 × 10^{-4} eV/K), β (145.1 K), and E_0 (1.56 eV) are constants chosen to be similar to literature-reported values for CdTe.[26] Throughout this paper, all the reported temperatures are based on BB peak energy as predicted by Equation 1. As shown in Figure 6, the E_g values decrease with increasing temperature for both the GIs and GBs; however, the extracted E_g for the GBs is generally lower than that for the GIs by 2.09 meV.

Since Se is known to reduce the bandgap, this finding suggests a slight aggregation of Se at the GBs.[1,27] Se composition can be estimated from the E_g measurements by the following relationship[28]:

$$E_g(\mathrm{CdSeTe}) = xE_g(\mathrm{CdSe}) + (1-x)E_g(\mathrm{CdTe}) - bx(1-x) \qquad \text{(Equation 2)}$$

where x is the Se composition and b is the bowing parameter. Using the accepted bandgap energies of 1.74 and 1.48 eV for CdSe and CdTe,[29,30] respectively, and b = 0.75, we found x = 11.05% for the mean of the GIs and x = 11.67% for the mean of the GBs.

Excitation-intensity-dependent PL spectra

Laser excitation-intensity-dependent PL measurements are often used to understand the nature of different transitions, such as excitonic, free-to-bound (FB), or

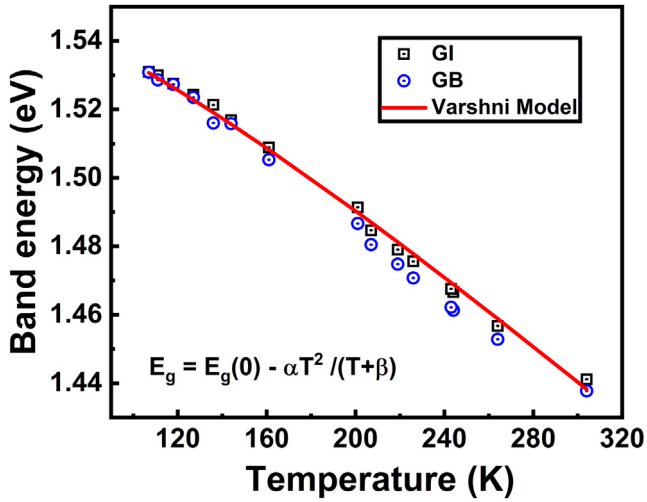

Figure 6. Bandgap energies with different temperatures

Bandgap energies for GIs and GBs with an estimated standard error of ±3.5 meV in the temperature range 107–161 K and error of ±3.0 meV in the temperature range 201–304 K.

DAP transitions in semiconductors.[31–33] Figure 7A shows the photon flux spectra for GB and GI sites at three different laser intensities and T = 107 K. From the plot, we can clearly observe three prominent sub-bandgap defect peaks at around 1.32, 1.37, and 1.42 eV, referred to as peak 1, peak 2, and peak 3, respectively. Defect peaks are slightly laser intensity dependent for both GI and GB luminescence, showing a slight blue shift with increasing intensity. To see this more clearly, all of the peaks were fitted to Gaussians, and the center peak position was plotted against the excitation intensity.

Figure 7B shows the excitation intensity vs. the defect peak energy for peaks 1, 2, and 3 for the GIs and peak 1 at the GBs on a log-linear plot (peaks 2 and 3 at the GB sites are too broad to be reliably extracted). An energy shift constant per decade of intensity (β) can be extracted using the following relation:[34]

$$I_{ex} = I_0 \exp(E_p / \beta) \quad \text{(Equation 3)}$$

where I_{ex} is the excitation intensity, E_p is the emission peak energy, and β is the energy shift constant. In general, it has been shown that an FB type of emission shows no significant change with excitation intensity, while a DAP transition shifts toward higher energies (blue shift) as the excitation intensity increases.[34] Since all three peaks shift toward higher energies, albeit by a small amount, we concluded that the observed sub-gap defect peaks originate from DAP transitions.

Cadmium vacancies (V_{Cd}), tellurium vacancies (V_{Te}), and Te_{Cd} are some of the major intrinsic defects in CdTe polycrystalline thin films.[35] In $CdCl_2$-treated CdTe films, Cl atoms normally substitute Te atoms, creating Cl_{Te}. This vacancy (Cl_{Te}) acts as a shallow donor. However, it also forms a complex (Cl_{Te}^{+}-V_{Cd}^{2-}) with a doubly negatively charged cadmium vacancy, which acts as a deep acceptor.[36,37] The Z band peaks (peaks at the lower energies, in our case, peak 1 and peak 2) are usually from this kind of DAP transition.[38] Thus, we believe that the low-energy DAP transition as shown in Figure 7A might be from V_{Te} as a donor and V_{Cd} and/or its complex as an acceptor. The intensity of this transition depends on the position and the capture cross section of the defects. Defect capture cross section and their energetic positions depend on the exact role of Se/Cl in the

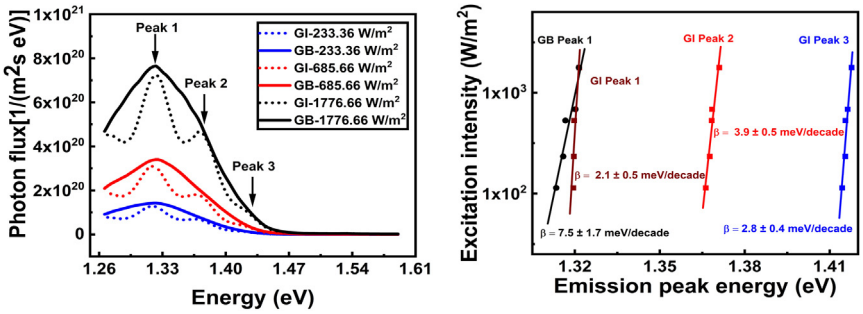

Figure 7. Results from intensity-dependent measurement

(A) Intensity-dependent PL spectra for both GI and GB.

(B) Energy shift constant per decade for the different peaks labeled in (A).

passivation mechanism, which needs to be further investigated. A similar observation was reported by Krustok et al.[39]; they observed that PL bands at lower energies are from the DAP transitions with V_{Te} acting as a donor. In another study,[40] using cathodoluminescence, the authors found a luminescence peak around 1.32 eV, which is similar to our peak 1 position. They also reported that this emission is consistent with DAP transitions in which the shallow donor is V_{Te} and V_{Cd} is the acceptor. In addition, another transition near 1.42 eV (peak 3) is also expected to be a DAP transition as confirmed by the excitation-intensity-dependent measurements.[41] This peak has been reported as a Cd-vacancy-related transition where V_{Cd} acts as a possible acceptor and Cl_{Te} as the donor. Several other reports confirm these findings[39,42] with an overall theme that these DAP transitions are generally attributed to V_{Cd}- and V_{Te}-related defects, although more recent theoretical work considering Cl and Cu (a common unintentional/intentional impurity) suggests additional complexes that could also be at play making assignment challenging.[43]

An important finding of our imaging results is that the energy shift parameter β for the GB emissions (peak 1) is significantly higher than that observed for the GIs. The β parameter is 7.5 ± 1.7 meV/decade for peak 1 in the GBs and 2.1 ± 0.5 meV/decade, 3.9 ± 0.5 meV/decade, and 2.8 ± 0.4 meV/decade for peak 1, peak 2, and peak 3 in the GIs, respectively. According to the model of Shklovskii and Efros,[44] the energy of an emitted photon in the DAP transition increases with a decrease in the surrounding potential fluctuations. In general, these potential fluctuations arise from the perturbations that oppositely charged defects of various concentrations create in the electrostatic potential.[45] Increasing the carrier concentration inside the material screens these electrostatic potential fluctuations, and hence a pronounced shift to a higher photon energy is observed.[46] An increase in β with an increase in carrier concentration was also reported by Phil Won Yu in various impurity-implanted GaAs films.[34] That work reported that β increases from 0.7 to 15 meV/decade with increasing carrier concentration from 10^{13} to 10^{18} cm^{-3}. Since β is higher for the signal coming from the GBs than the GIs in our images, we therefore conclude that the local carrier concentration must be higher at the GB sites than grain interiors. This is not surprising given that GBs are areas of crystalline discontinuity from one grain to the next, and stronger potential fluctuations at these interfaces are expected. Note that without the high spectral and spatial resolution of the hyperspectral imaging microscope, these conclusions could not be easily made and therefore show the power of this technique. These excitation-dependent local variations are consistent with the PEEM results discussed in the next section.

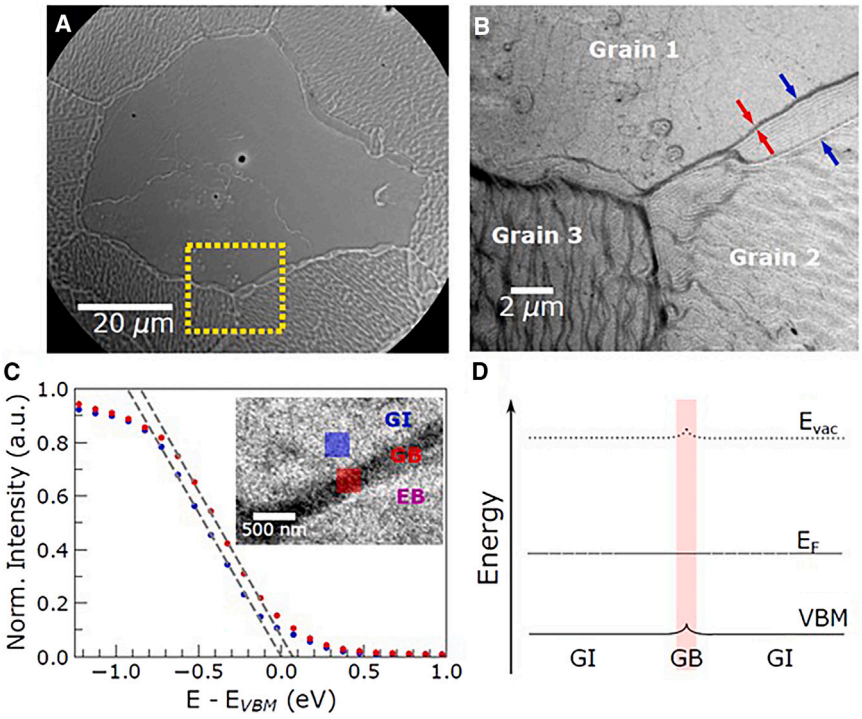

Figure 8. PEEM observation of GBs

(A) Low-magnification PEEM image of an entire grain.

(B) Higher-magnification PEEM image of the area marked by the dashed yellow box in (A) at the boundary of three grains. One grain boundary is marked by a pair of red arrows, while a non-uniform EB region is marked by a pair of blue arrows.

(C) Averaged photoemission spectrum from the GI (blue) and GB (red) regions indicated in the inset. The dashed gray lines are linear fits to the valence band maximum edge, giving a relative shift of approximately 70 meV

(D) Surface band diagram comparing GI and GB energy structure. The Fermi energy and vacuum level are denoted as E_F and E_{vac}, respectively. The gray scale of the images is the photoemission intensity (e.g., white means higher photoemission intensity).

PEEM of grains and GBs

PEEM measurements were performed on the CdSeTe thin films to understand the differences in the local surface electronic structure at the GBs compared to the GIs. At low magnifications, PEEM can readily identify the grains and boundaries, as shown in Figure 8A. We note that there are slight differences in the grain-to-grain topography with small wrinkle-like features occasionally visible, corresponding to different crystal growth orientations, consistent with the PL intragranular features discussed above.[47] At higher magnification, the surface features at the GBs are visible. The GBs are visible as dark lines in PEEM, shown by the red arrows in Figure 8B, indicating that the surface morphology at the boundary is not flat. In addition, the GBs are often next to or surrounded by a non-uniform "extended boundary" (EB) up to 2 μm wide (marked by blue arrows in Figure 8B), where the surface topography is different from the GI. We then measure the photoemission spectrum from the GB and compare it to the GI, as shown in Figure 8C. There is a shift in the photoemission spectrum of approximately 70 meV to higher energy for the GBs, compared to the GIs. This value is comparable to barrier heights reported for different CdTe growth and $CdCl_2$ treatment conditions.[37,48] The entire spectrum, including the cutoff (not shown) shifts by the same amount, indicating a rigid shift

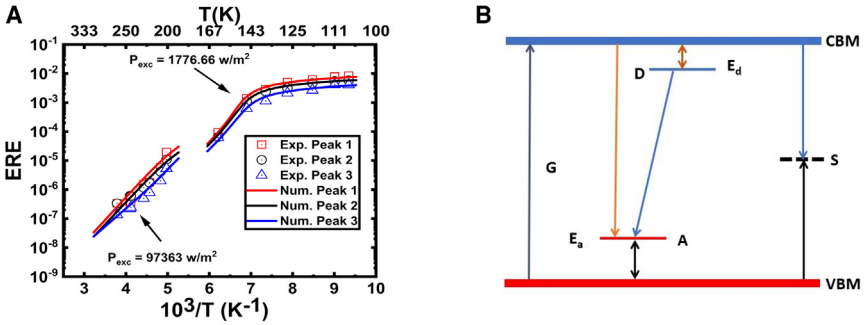

Figure 9. ERE vs. T plot and the radiative and non-radiative transition process

(A) Thermal quenching of the ERE for peak 1, peak 2, and peak 3 from the GIs along with numerical modeling based on the rate-equation model by Reshchikov[52] (solid lines).

(B) A simplified schematic of the various radiative and non-radiative transitions that are the basis of this model where A, D, G, and S are the acceptor, donor, generation rate, and the unknown deep donor respectively.

in the band structure and work function (vacuum level) at the GB, as illustrated in Figure 8D. This band alignment suggests that holes could be funneled or collected at the GB due to the slight VBM band offset. This supports our PL-derived result that β is higher at the GBs compared to the GIs, because a higher carrier concentration at the GB screens the local potential fluctuations and causes a greater shift of the DAP peak positions with excitation intensity. This type of band offset has been suggested to increase the collection efficiency in CdTe solar cells because of minority carrier repulsion due to the increased hole population at the GB.[49] However, environmental factors, such as adsorbed oxygen, are known to affect the work function and band bending at CdTe GBs. In other work, a downward band bending in the VBM at the site of GBs has also been reported.[50] The PEEM result showing an upward band bending at GBs at the very least indicates that the GBs are slightly more p doped than the GIs. In general, it is difficult here to pinpoint the origin of the GB band bending.

PL quenching and rate-equation model

Next, we discuss the dramatic temperature-dependent PL results that we showed in the series of images in Figure 2. Here, a convenient figure of merit is the ERE, defined as the ratio of emitted (luminescence) photons to incident (excitation) photons, with an ERE = 1 corresponding to 100% PL efficiency. Since the hyperspectral imaging technique gives the local absolute spectral photon flux, we can choose to calculate the ERE over different spectral regions such as the BB peak or the defect peaks. Here, we focus on the temperature dependence of the DAP-related ERE but we also extracted the band-band ERE vs. T and show those results in Figure S2. Figure 9A shows a plot of the DAP-related ERE vs. inverse temperature in the spectral range from 830 to 1,000 nm, i.e., the three main GI defect peaks shown earlier, and ignoring any other transitions that could exist at wavelengths longer than 1,000 nm. The PL temperature dependence of the GB peak is similar to the GI peaks and is shown in Figure S3. An abrupt thermal quenching of ERE (almost five orders of magnitude change) was observed in the CdSeTe thin film. The discontinuity in the graph is due to the limitations in our measurement. At low excitation (in our case, 1,776 W/m^2), we could not get sufficient photon emission signal at higher temperatures. We therefore increased the excitation power to 97 kW/m^2 to increase the signal strength. From Figure 9A, it is clear that a transition takes place at around 156 K. This temperature is called the characteristic temperature at which point

defect species can switch from a near-equilibrium population of levels to a population inversion at higher temperatures (i.e., going from a radiative recombination channel to a non-radiative recombination channel). This kind of abrupt thermal quenching has been reported in highly resistive semiconductors[17,51] and is not specific to CdSeTe thin films.

To understand this behavior better, a rate-equation model based on the treatment by Reshchikov is used here; see Figure S1 and Note S1 for all the equations and model parameters used to calculate the solid lines shown in Figure 9A.[53] According to this model, point defects of three major types, acceptors (A), donors (D), and unknown non-radiative deep donors (S) with total concentrations N_A, N_D, and N_S, respectively, are responsible for sub-bandgap PL emission. The ionization energies for the donor and acceptor states are E_D and E_A, whereas the non-radiative center S has deep levels, so the thermal emission of charge carriers from it can be ignored. The capture coefficients for donor, acceptor, and non-radiative defects are $C_{D,}$ C_A, and C_S, respectively. When the sample is illuminated with excitation power density P_{exc}, electron-hole pairs are excited with generation rate G. Photogenerated electrons and holes are captured by shallow donors and acceptors, respectively. These capturing transitions can be either fast and non-radiative through S or the carriers can tunnel between D and A. The pathway probabilities depend on the sizes of the electron and hole wave functions and the separation distance between D and A.

At low temperatures, the probability of the DAP transition is much higher than the probability for photogenerated electrons to be captured directly by a neutral acceptor. This is because the concentration of free electrons is much lower than the concentration of electrons bound to shallow donors. At higher temperatures, in our case $T > 156$ K, the thermal emission of holes from the acceptor level to the valence band becomes significant and increases exponentially with temperature, proportional to $\exp(-E_A/kT)$. When the thermal energy is sufficient, non-radiative centers actively participate in the capture of electrons or holes from either band. Due to this sudden drop of electron concentration, recombination abruptly changes from radiative to non-radiative and hence quenches the PL emission that was due to the DAPs. At low temperatures (i.e., temperatures less than the characteristic temperature), PL intensity is not very sensitive to the electron-capture coefficient, but, at temperatures higher than the characteristic temperature, PL intensity is inversely proportional to the electron-capture coefficient. It is observed that, for a significant and abrupt drop in the PL intensity to occur, non-radiative centers (S) with large electron-capture coefficients must be present.[17] As a point of contrast, higher-quality, lower-defect-density films of CdTe do not show such dramatic PL quenching behavior.[53] Figure 9B shows a simplified schematic of the various electron and hole transitions that are possible between these three types of defects.

As there are many parameters in this model, some were estimated from other works on similar kinds of samples, and others were constrained to be within physically reasonable ranges. The solutions to this model are shown in Figure 9A as solid lines. With some restrictions (i.e., at low temperatures), only photogenerated electrons and holes are present (i.e., there are not thermally excited carriers) and neglecting high large-carrier-density effects such as Auger recombination, degenerate doping, and stimulated emission, the numerical model matches well with our experimental data and shows the same abrupt PL quenching behavior.

Implication for devices

The findings reported here on the GI and GB luminescence and electronic band structure properties of CGG-grown CdSeTe films provide an interesting case study for use of spatially resolved spectral imaging techniques in examining local recombination properties of these and other thin-film polycrystalline materials such as chalcogenides and perovskites. Combining the temperature-dependent hyperspectral and PEEM imaging techniques has revealed that band bending at the GBs leads to a higher carrier concentration at these locations. These excess carriers could screen local potential fluctuations, determined to be on the order of 10–20 meV, which in turn lead to a noticeable higher-energy shift in the PL signal. These findings, along with the observation of a lower non-radiative recombination at the GBs, indicate that GBs, at least in this material system, play a more beneficial role in carrier collection and transport across the film.

Given that the ultimate goal of these CGG films is to serve as a growth template for achieving large-grained CdTe films in a superstrate device structure, their defect-mediated luminescence, local band bending, and recombination characteristics are consequential to the operation of a full photovoltaic (PV) device. After all, much of the light absorption and carrier generation will take place in the CGG template below the CdTe layer. However, even if a CGG CdSeTe template is made much thinner, the charge carriers would still have to transport through the CdSeTe layer to reach the CdTe. Therefore, the recombination phenomena discussed here will surely affect carriers, particularly near the maximum power point or at V_{oc}, where the electric field is weaker across the junction. Hence, it is important that the CdSeTe template layer, within the device stack, also possesses a low defect density and good interfacial properties so that it will not turn into a current- or voltage-limiting layer. So, the costs and benefits of giant crystalline grains versus additional recombination losses will need to be investigated on the full device structure, but these CGG-only films have provided a baseline for what to expect. In their current form, these CdSeTe films would perform poorly as an active layer within a full device stack given the low room-temperature ERE of these films, but further improvements in defect passivation should result in improved optoelectronic properties in the future.

Interestingly, the absolute PL measurements do show a forward path for incorporation of CGG films as the main absorber layer within a device structure despite the low Se content. The fact that the ERE values are so much higher at lower temperatures implies that the internal V_{oc} will be much higher at low temperatures beyond its normal temperature dependence as predicted by the detailed balance. If the mid-gap defect states can be better passivated, the ERE near room temperature will also be substantially increased, making the material a viable active layer in a device structure with its beneficial large-grain structure.

Wide-field hyperspectral imaging in PL mode was successfully employed to visualize the luminescence emission variations between GIs and GBs in CdSeTe thin film prepared by the CGG method. The origin of several sub-bandgap emission peaks was attributed to DAP transitions, and it was observed that these transitions exhibit higher luminescence rates at the GBs than within the GIs. The reason for this higher luminescence signal at the GBs was attributed to a better non-radiative defect passivation at the GBs due to a higher concentration of Se and/or Cl. The energy shift constant was found to be locally higher at the GBs than GIs, suggesting a higher carrier concentration at the GBs. Furthermore, this observation was validated by PEEM imaging, showing upward band bending at

the GB sites with an approximately 70-meV higher VBM for GBs compared to GIs. The dramatic quenching of the PL radiative efficiency was explained by a numerical solution to a recent rate-equation model and further attributes the origin of the strong PL emission in this material to an interplay of radiative and non-radiative recombination channels through the existence of a variety of donor-acceptor states.

EXPERIMENTAL PROCEDURES

Resource availability

Lead contact

Further information and requests for resources should be directed to and will be fulfilled by the lead contact, Dr. Behrang Hamadani (behrang.hamadani@nist.gov).

Materials availability

This study did not generate any new unique materials.

Data availability

The data used during this study are available from the lead author upon reasonable request.

Sample fabrication and characterization

The sample studied here consists of a large-grain (100–200 μm lateral dimension) polycrystalline thin film of $CdSe_{0.1}Te_{0.9}$ formed on an alumina-coated glass substrate. The CdSeTe films used in this study are unusual given the exceptionally high grain size/film thickness ratio. The large-grain-size CdSeTe film studied here was made by the CGG process. A 3.0-μm CdSeTe precursor film was evaporated onto a 0.7-mm-thick alumino-borosilicate glass (Corning 7059) substrate coated with 100 nm of alumina heated to about 400°C. Evaporation was from a single-source alumina crucible containing an alloy of $CdSe_{0.1}Te_{0.9}$ (5N Plus) heated to 660°C to produce a deposition flux close to 10 Å/s. The as-deposited grain size at this point was only about 200 nm. In the subsequent CGG step, the CdSeTe precursor film was then heated to 550°C while suspended 1 mm, film-side down, above a Se-containing powder (typically, $CdSe_{0.4}Te_{0.6}$) in an atmosphere of 100-Torr helium. The net effect was a three-order magnitude increase in CdSeTe grain size and a morphology shown in Figure 2. Details about the CGG process can be found in a previous report.[5] Though the conversion mechanism needs further study, it appears similar to explosive recrystallization where solid films first melt and then rapidly spread solidify into many larger-grained films. In this case, the latent heat associated with the energy of melting is believed to be the result of the amorphous-crystalline phase transition reported for Se-Te alloys.[54] After the CGG step, the CdSeTe film was then annealed and suspended over a powder of $CdCl_2$ at 550°C for 10 min in an ambient of 400-Torr helium to increase luminescence efficiency.

HS imaging in PL mode was performed using a wide-field imaging system from Photon ETC. All images were obtained under a 20× magnification by scanning in the spectral region of 780–980 nm and recording the images using the sCMOS camera. The spectral resolution is around 2 nm, and the spatial resolution is ≈1 μm. For PL excitation, a 532-nm laser is used to uniformly illuminate the cell from the free surface side, with excitation intensities as reported in the text. The calibration of the imager to obtain absolute photon flux rates is discussed elsewhere.[55] Temperature-dependent imaging was performed with a liquid-nitrogen-flow optical cryostat under vacuum from 300 to 77 K. The relative uncertainties of the PL flux rates presented here are about ±15%. Wavelength calibration of the HS system was performed with pen lights and is accurate to within 1 nm.

PEEM measurements were carried out using a setup described previously.[56] The base pressure of the measurement chamber was below 10^{-9} bar. The illumination source was the fourth harmonic of a titanium: sapphire laser at either 210 nm (5.9 eV) or 192 nm (6.5 eV) with a nominal intensity of 3 Wm^{-2} at the sample. The sample was simultaneously illuminated with filtered (Corning #2418 colored glass filter) light from a mercury lamp to promote photoconductivity and prevent sample charging. High-magnification PEEM images used a 20-μm (contrast) aperture that angularly restricts the photoelectrons to ≈1.1 mrad. Energy-resolved PEEM images were acquired by placing a 2-μm slit at the entrance of the PEEM magnetic prism to act as the analyzer entrance slit, while the contrast aperture was used as the exit slit, giving an overall imaging energy resolution of approximately 1 eV. Images were acquired while changing the sample potential in steps of 100 meV to capture the entire photoemission spectrum. A reference spectrum on a relatively uniform area of the sample was taken immediately after the first spectrum stack and used to correct for the non-isochromaticity of the magnetic prism by using the peak position of the reference spectrum at each image pixel. All PEEM images were corrected for a non-uniform detector response using a standard flat field and dark image method.

SUPPLEMENTAL INFORMATION

Supplemental information can be found online at https://doi.org/10.1016/j.xcrp.2023.101522.

ACKNOWLEDGMENTS

The authors thank Professor Heayoung Yoon of the University of Utah for useful discussions and H. Moutinho of NREL for the EBSD images in the supplement. This work was authored in part by the National Renewable Energy Laboratory, operated by Alliance for Sustainable Energy, LLC, for the US Department of Energy (DOE) under contract no. DE-AC36-08GO28308. Funding provided by the US Department of Energy Office of Energy Efficiency and Renewable Energy Solar Energy Technologies Office. The views expressed in the article do not necessarily represent the views of the DOE or the US Government. The US Government retains, and the publisher, by accepting the article for publication, acknowledges that the US Government retains, a nonexclusive, paid-up, irrevocable, worldwide license to publish or reproduce the published form of this work, or allow others to do so, for US Government purposes. NIST disclaimer: certain commercial equipment, instruments, software, or materials are identified in this paper to specify the experimental procedure adequately. Such identification is not intended to imply recommendation or endorsement by the National Institute of Standards and Technology, nor is it intended to imply that the materials or equipment identified are necessarily the best available for the purpose.

AUTHOR CONTRIBUTIONS

G.R.N. performed the hyperspectral PL measurements, characterization, and analysis of the PL results and authored the paper. A.J.W. performed the PEEM measurements and analysis. D.S.A. and J.N.D. grew the CdSeTe films. M.O.R., S.J.P., and S.M.T. made significant conceptual contributions and supported laboratory measurements. N.M.P. developed the numerical rate-equation model used in this work. B.H.H. contributed to the PL measurements and analysis and supervised the work. All the authors joined in the discussions and commented on the manuscript.

DECLARATION OF INTERESTS

The authors declare no competing interests.

Received: March 28, 2023
Revised: June 23, 2023
Accepted: July 7, 2023
Published: August 4, 2023

REFERENCES

1. Wang, R., Lan, M., and Wei, S.-H. (2021). Enhanced performance of Se-alloyed CdTe solar cells: the role of Se-segregation on the grain boundaries. J. Appl. Phys. *129*, 024501. https://doi.org/10.1063/5.0036701.

2. Fiducia, T.A.M., Mendis, B.G., Li, K., Grovenor, C.R.M., Munshi, A.H., Barth, K., Sampath, W.S., Wright, L.D., Abbas, A., Bowers, J.W., et al. (2019). Understanding the role of selenium in defect passivation for highly efficient selenium-alloyed cadmium telluride solar cells. Nat. Energy *4*, 526. https://doi.org/10.1038/s41560-019-0416-0.

3. Lee, J.-W., Bae, S.-H., de Marco, N., Hsieh, Y.-T., Dai, Z., and Yang, Y. (2018). The role of grain boundaries in perovskite solar cells. Mater. Today Energy *7*, 149–160. https://doi.org/10.1016/j.mtener.2017.07.014.

4. Nazem, H., Dizaj, H.P., and Gorji, N.E. (2019). Modeling of J sc and V oc versus the grain size in CdTe, CZTS and Perovskite thin film solar cells. Superlattice. Microstruct. *128*, 421–427. https://doi.org/10.1016/j.spmi.2019.02.002.

5. Albin, D.S., Amarasinghe, M., Reese, M.O., Moseley, J., Moutinho, H., and Metzger, W.K. (2021). Colossal grain growth in Cd(Se,Te) thin films and their subsequent use in CdTe epitaxy by close-spaced sublimation. J. Phys. Energy *3*, 024003. https://doi.org/10.1088/2515-7655/abd297.

6. Munshi, A.H., Kephart, J.M., Abbas, A., Danielson, A., Gēlinas, G., Beaudry, J.N., Barth, K.L., Walls, J.M., and Sampath, W.S. (2018). Effect of CdCl2 passivation treatment on microstructure and performance of CdSeTe/CdTe thin-film photovoltaic devices. Sol. Energy Mater. Sol. Cell. *186*, 259–265. https://doi.org/10.1016/j.solmat.2018.06.016.

7. Tuteja, M., Koirala, P., Palekis, V., MacLaren, S., Ferekides, C.S., Collins, R.W., and Rockett, A.A. (2016). Direct observation of CdCl 2 treatment induced grain boundary carrier depletion in CdTe solar cells using scanning probe microwave reflectivity based capacitance measurements. J. Phys. Chem. C *120*, 7020–7024. https://doi.org/10.1021/acs.jpcc.6b00874.

8. Kavanagh, S.R., Walsh, A., and Scanlon, D.O. (2021). Rapid recombination by cadmium vacancies in CdTe. ACS Energy Lett. *6*, 1392–1398. https://doi.org/10.1021/acsenergylett.1c00380.

9. Selvaraj, S.C., Gupta, S., Caliste, D., and Pochet, P. (2021). Passivation mechanism in CdTe solar cells: the hybrid role of Se. Appl. Phys. Lett. *119*, 062105. https://doi.org/10.1063/5.0058290.

10. Bidaud, T., Moseley, J., Amarasinghe, M., Al-Jassim, M., Metzger, W.K., and Collin, S. (2021). Imaging CdCl2 defect passivation and formation in polycrystalline CdTe films by cathodoluminescence. Phys. Rev. Mater. *5*, 064601. https://doi.org/10.1103/PhysRevMaterials.5.064601.

11. Kuciauskas, D., Dippo, P., Kanevce, A., Zhao, Z., Cheng, L., Los, A., Gloeckler, M., and Metzger, W.K. (2015). The impact of Cu on recombination in high voltage CdTe solar cells. Appl. Phys. Lett. *107*, 243906. https://doi.org/10.1063/1.4938127.

12. Kuciauskas, D., Li, S., Moseley, J., Albin, D., Lee, C., Onno, A.L., and Holman, Z.C. (2022). Voltage loss comparison in CdSe/CdTe solar cells and polycrystalline CdSeTe heterostructures. IEEE J. Photovolt. *12*, 6–10. https://doi.org/10.1109/JPHOTOV.2021.3117914.

13. Hamadani, B.H., Stevens, M.A., Conrad, B., Lumb, M.P., and Schmieder, K.J. (2022). Visualizing localized, radiative defects in GaAs solar cells. Sci. Rep. *12*, 14838. https://doi.org/10.1038/s41598-022-19187-4.

14. Lin, L., Chen, C., and Xu, T. (2020). Spatial-spectral hyperspectral image classification based on information measurement and CNN. EURASIP J. Wirel. Commun. Netw. *2020*, 59. https://doi.org/10.1186/s13638-020-01666-9.

15. Bube, R.H. (1993). A new mechanism for superlinear photoconductivity with relevance to amorphous silicon. J. Appl. Phys. *74*, 5138–5143. https://doi.org/10.1063/1.355310.

16. Julkarnain, M., Fukuda, T., Kamata, N., and Arakawa, Y. (2016). Below-gap emission bands in undoped GaN and its excitation density dependence. Phys. Status Solidi C *13*, 242–244. https://doi.org/10.1002/pssc.201510190.

17. Reshchikov, M.A. (2014). Temperature dependence of defect-related photoluminescence in III-V and II-VI semiconductors. J. Appl. Phys. *115*, 012010. https://doi.org/10.1063/1.4838038.

18. Guo, J., Sen, F.G., Mannodi-Kannakithodi, A., Barnard, E.S., Sampath, W., Munshi, A., Chan, M.K.Y., and Klie, R.F. (2019). Study of effects of Cl and Se in CdSeTe solar cells using scanning transmission electron microscopy. Microsc. Microanal. *25*, 2150–2151. https://doi.org/10.1017/S1431927619011486.

19. Katahara, J.K., and Hillhouse, H.W. (2014). Quasi-Fermi level splitting and sub-bandgap absorptivity from semiconductor photoluminescence. J. Appl. Phys. *116*, 173504. https://doi.org/10.1063/1.4898346.

20. Tong, C.-J., and McKenna, K.P. (2019). Passivating grain boundaries in polycrystalline CdTe. J. Phys. Chem. C Nanomater. Interfaces *123*, 23882–23889. https://doi.org/10.1021/acs.jpcc.9b08373.

21. Feng, C., Yin, W.-J., Nie, J., Zu, X., Huda, M.N., Wei, S.-H., Al-Jassim, M.M., and Yan, Y. (2012). Possible effects of oxygen in Te-rich Σ3 (112) grain boundaries in CdTe. Solid State Commun. *152*, 1744–1747. https://doi.org/10.1016/j.ssc.2012.05.006.

22. Zhang, L., da Silva, J.L.F., Li, J., Yan, Y., Gessert, T.A., and Wei, S.-H. (2008). Effect of copassivation of Cl and Cu on CdTe grain boundaries. Phys. Rev. Lett. *101*, 155501. https://doi.org/10.1103/PhysRevLett.101.155501.

23. Sen, F.G., Mannodi-Kanakkithodi, A., Paulauskas, T., Guo, J., Wang, L., Rockett, A., Kim, M.J., Klie, R.F., and Chan, M.K. (2021). Computational design of passivants for CdTe grain boundaries. Sol. Energy Mater. Sol. Cell. *232*, 111279. https://doi.org/10.1016/j.solmat.2021.111279.

24. Durose, K., Cousins, M.A., Boyle, D.S., Beier, J., and Bonnet, D. (2002). Grain boundaries and impurities in CdTe/CdS solar cells. Thin Solid Films *403–404*, 396–404. https://doi.org/10.1016/S0040-6090(01)01518-8.

25. Varshni, Y.P. (1967). Temperature dependence of the energy gap in semiconductors. Physica *34*, 149–154. https://doi.org/10.1016/0031-8914(67)90062-6.

26. Allahverdi, Ç., and Yükselici, M.H. (2008). Temperature dependence of absorption band edge of CdTe nanocrystals in glass. New J. Phys. *10*, 103029. https://doi.org/10.1088/1367-2630/10/10/103029.

27. Shah, A., Nicholson, A.P., Fiducia, T.A.M., Abbas, A., Pandey, R., Liu, J., Grovenor, C., Walls, J.M., Sampath, W.S., and Munshi, A.H. (2021). Understanding the copassivation effect of Cl and Se for CdTe grain boundaries. ACS Appl. Mater. Interfaces *13*, 35086–35096. https://doi.org/10.1021/acsami.1c06587.

28. Lingg, M., Spescha, A., Haass, S.G., Carron, R., Buecheler, S., and Tiwari, A.N. (2018). Structural and electronic properties of CdTe 1-x Se x films and their application in solar cells. Sci. Technol. Adv. Mater. *19*, 683–692. https://doi.org/10.1080/14686996.2018.1497403.

29. Wei, S.-H., Zhang, S.B., and Zunger, A. (2000). First-principles calculation of band offsets, optical bowings, and defects in CdS, CdSe, CdTe, and their alloys. J. Appl. Phys. *87*, 1304–1311. https://doi.org/10.1063/1.372014.

30. Yang, J., and Wei, S.-H. (2019). First-principles study of the band gap tuning and doping control in CdSe x Te 1−x alloy for high efficiency solar cell. Chin. Phys. B *28*, 086106. https://doi.org/10.1088/1674-1056/28/8/086106.

31. Reshchikov, M.A., and Morkoç, H. (2005). Luminescence properties of defects in GaN. J. Appl. Phys. *97*, 061301. https://doi.org/10.1063/1.1868059.

32. Dingle, R., and Ilegems, M. (1971). Donor-acceptor pair recombination in GaN. Solid State Commun. *9*, 175–180. https://doi.org/10.1016/0038-1098(71)90112-8.

33. Schmidt, T., Lischka, K., and Zulehner, W. (1992). Excitation-power dependence of the near-band-edge photoluminescence of semiconductors. Phys. Rev. B *45*, 8989–8994. https://doi.org/10.1103/PhysRevB.45.8989.

34. Yu, P.W. (2008). Excitation-dependent emission in Mg-Be-Cd-and Zn-implanted GaAs. J. Appl. Phys. *48*, 5043–5051.

35. Yang, J.-H., Yin, W.-J., Park, J.-S., Ma, J., and Wei, S.-H. (2016). Review on first-principles study of defect properties of CdTe as a solar cell absorber. Semicond. Sci. Technol. *31*, 083002. https://doi.org/10.1088/0268-1242/31/8/083002.

36. Burgelman, M. (2006). Cadmium telluride thin film solar cells: characterization, fabrication and modeling. In Thin Film Solar Cells (John Wiley & Sons, Ltd), pp. 277–324. https://doi.org/10.1002/0470091282.ch7.

37. Vigil-Galán, O., Vaillant, L., Mendoza-Pérez, R., Contreras-Puente, G., Vidal-Larramendi, J., and Morales-Acevedo, A. (2001). Influence of the growth conditions and postdeposition treatments upon the grain boundary barrier height of CdTe thin films deposited by close space vapor transport. J. Appl. Phys. *90*, 3427–3431. https://doi.org/10.1063/1.1400090.

38. Kvit, A.v., Klevkov, Y.v., Medvedev, S.A., Bagaev, V.S., Perestoronin, A.v., and Plotnikov, A.F. (2000). Evolution of photoluminescence spectra of stoichiometric CdTe: Dependence on the purity of starting components. Semiconductors *34*, 17–20. https://doi.org/10.1134/1.1187955.

39. Krustok, J., Valdna, V., Hjelt, K., and Collan, H. (1996). Deep center luminescence in p -type CdTe. J. Appl. Phys. *80*, 1757–1762. https://doi.org/10.1063/1.362981.

40. Moseley, J., Al-Jassim, M.M., Moutinho, H.R., Guthrey, H.L., Metzger, W.K., and Ahrenkiel, R.K. (2013). Explanation of red spectral shifts at CdTe grain boundaries. Appl. Phys. Lett. *103*, 233103. https://doi.org/10.1063/1.4838015.

41. Collins, S., Vatavu, S., Evani, V., Khan, M., Bakhshi, S., Palekis, V., Rotaru, C., and Ferekides, C. (2015). Radiative recombination mechanisms in CdTe thin films deposited by elemental vapor transport. Thin Solid Films *582*, 139–145. https://doi.org/10.1016/j.tsf.2014.11.088.

42. de Nobel, D. (1959). Phase equilibria and semiconducting properties of cadmium telluride *). R 380 reprinted from philips. Res. Repts *14*, 361–399.

43. Krasikov, D., and Sankin, I. (2017). Defect interactions and the role of complexes in the CdTe solar cell absorber. J. Mater. Chem. A Mater. *5*, 3503–3513. https://doi.org/10.1039/C6TA09155E.

44. Shklovskii, B., and Efros, A. (1984). Electronic Properties of Doped Semiconductors (Berlin: Springer).

45. Shrestha, N., Song, Z., Chen, C., Bastola, E., Wang, X., Yan, Y., and Ellingson, R.J. (2020). Charge compensating defects in methylammonium lead iodide perovskite suppressed by formamidinium inclusion. J. Phys. Chem. Lett. *11*, 121–128. https://doi.org/10.1021/acs.jpclett.9b03234.

46. Romero, M.J., Ramanathan, K., Contreras, M.A., Al-Jassim, M.M., Noufi, R., and Sheldon, P. (2003). Cathodoluminescence of Cu(In,Ga) Se2 thin films used in high-efficiency solar cells. Appl. Phys. Lett. *83*, 4770–4772. https://doi.org/10.1063/1.1631083.

47. Amarasinghe, M., Albin, D., Kuciauskas, D., Moseley, J., Perkins, C.L., and Metzger, W.K. (2021). Mechanisms for long carrier lifetime in Cd(Se)Te double heterostructures. Appl. Phys. Lett. *118*, 1–6. https://doi.org/10.1063/5.0047976.

48. Berg, M., Kephart, J.M., Munshi, A., Sampath, W.S., Ohta, T., and Chan, C. (2018). Local electronic structure changes in polycrystalline CdTe with CdCl 2 treatment and air exposure. ACS Appl. Mater. Interfaces *10*, 9817–9822. https://doi.org/10.1021/acsami.7b18963.

49. Brooks, W.S.M., Irvine, S.J.C., and Taylor, D.M. (2013). Scanning Kelvin probe measurements on As-doped CdTe solar cells. Semicond. Sci. Technol. *28*, 105024. https://doi.org/10.1088/0268-1242/28/10/105024.

50. Major, J.D. (2016). Grain boundaries in CdTe thin film solar cells: a review. Semicond. Sci. Technol. *31*, 093001. https://doi.org/10.1088/0268-1242/31/9/093001.

51. Reshchikov, M.A., Olsen, A.J., Bishop, M.F., and McMullen, T. (2013). Superlinear increase of photoluminescence with excitation intensity in Zn-doped GaN. Phys. Rev. B *88*, 075204. https://doi.org/10.1103/PhysRevB.88.075204.

52. Reshchikov, M.A., Kvasov, A.A., Bishop, M.F., McMullen, T., Usikov, A., Soukhoveev, V., and Dmitriev, V.A. (2011). Tunable and abrupt thermal quenching of photoluminescence in high-resistivity Zn-doped GaN. Phys. Rev. B *84*, 075212. https://doi.org/10.1103/PhysRevB.84.075212.

53. Kuciauskas, D., Dippo, P., Zhao, Z., Cheng, L., Kanevce, A., Metzger, W.K., and Gloeckler, M. (2016). Recombination analysis in cadmium telluride photovoltaic solar cells with photoluminescence spectroscopy. IEEE J. Photovolt. *6*, 313–318. https://doi.org/10.1109/JPHOTOV.2015.2483366.

54. Vermeulen, P.A., Momand, J., and Kooi, B.J. (2014). Reversible amorphous-crystalline phase changes in a wide range of Se 1−x Te x alloys studied using ultrafast differential scanning calorimetry. J. Chem. Phys. *141*, 024502. https://doi.org/10.1063/1.4886185.

55. Chavali, S.M., Roller, J., Dagenais, M., and Hamadani, B.H. (2022). A comparative study of subcell optoelectronic properties and energy losses in multijunction solar cells. Sol. Energy Mater. Sol. Cell. *236*, 111543. https://doi.org/10.1016/j.solmat.2021.111543.

56. Niefind, F., Bell, H.G., Mai, T., Hight Walker, A.R., Elmquist, R.E., and Pookpanratana, S. (2022). Imaging and measuring the electronic properties of epitaxial graphene with a photoemission electron microscope. J. Appl. Phys. *131*, 015303. https://doi.org/10.1063/5.0076145.